Commun. Comput. Phys.
doi: 10.4208/cicp.030210.051110a

Vol. **10**, No. 2, pp. 339-370
August 2011

Convergent Adaptive Finite Element Method Based on Centroidal Voronoi Tessellations and Superconvergence

Yunqing Huang[1,*], Hengfeng Qin[2], Desheng Wang[3] and
Qiang Du[4]

[1] *Hunan Key Laboratory for Computation and Simulation in Science and Engineering, Xiangtan University, Hunan 411105, China.*
[2] *Department of Mechanical and Electronic Engineering, School of Mechanical Engineering, Xiangtan University, Hunan 411105, China.*
[3] *Division of Mathematical Sciences, School of Physical and Mathematical Sciences, Nanyang Technological University, Singapore 637371, Singapore.*
[4] *Department of Mathematics, Pennsylvania State University, University Park, PA 16802, USA.*

Received 3 February 2010; Accepted (in revised version) 5 November 2010

Communicated by Pingwen Zhang

Abstract. We present a novel adaptive finite element method (AFEM) for elliptic equations which is based upon the Centroidal Voronoi Tessellation (CVT) and superconvergent gradient recovery. The constructions of CVT and its dual Centroidal Voronoi Delaunay Triangulation (CVDT) are facilitated by a localized Lloyd iteration to produce almost equilateral two dimensional meshes. Working with finite element solutions on such high quality triangulations, superconvergent recovery methods become particularly effective so that asymptotically exact a posteriori error estimations can be obtained. Through a seamless integration of these techniques, a convergent adaptive procedure is developed. As demonstrated by the numerical examples, the new AFEM is capable of solving a variety of model problems and has great potential in practical applications.

AMS subject classifications: 65N50, 65N15

Key words: Finite element methods, superconvergent gradient recovery, Centroidal Voronoi Tessellation, adaptive methods.

1 Introduction

Adaptive finite element methods (AFEM) have been widely studied for over two decades and are now standard tools in numerical simulations of scientific and engineering prob-

---

*Corresponding author. *Email addresses:* `huangyq@xtu.edu.cn` (Y. Huang), `qinhf2001@yahoo.com.cn` (H. Qin), `desheng@ntu.edu.sg` (D. Wang), `qdu@math.psu.edu` (Q. Du)

lems [1, 2, 28, 35, 45]. AFEMs are especially attractive for problems with solutions which are of singular or multi-scale nature [1, 3, 8, 10, 38]. A standard adaptive finite element method for solving a partial differential equation (PDE) consists of iterations between several key components: *SOLVE* → *ERROR ESTIMATE* → *SIZING MODIFY* → *REFINE/COARSEN*. More specifically, the procedure *SOLVE* solves for the discrete finite element solution of the PDE on the current mesh; the procedure *ERROR ESTIMATE* performs a posteriori error estimation over the computed finite element solution; with the computed a posteriori estimate, the procedure *SIZING MODIFY* introduces the new mesh sizing based on an error equal distribution principle; and the procedure *REFINE /COARSEN* changes the mesh through moving and/or inserting/removing vertices together with other compatible element modifications. The convergence of an adaptive finite element algorithm implies that, starting from a given coarse mesh, the adaptation loop converges within a prescribed error tolerance in a finite number of iterations.

To develop a robust and convergent adaptive finite element method for elliptic problems on a complicated geometry, it is necessary to construct reliable a posteriori error estimates and effective element marking (for refinement/coarsening) strategy, along with suitable mesh sizing modification and effective mesh refinement and optimization. While various techniques have been developed to address each of the above issues, we present a new approach in this work for the adaptive finite element solution of two dimensional elliptic equations. The main ideas underneath our method consist of the use of superconvergence properties of the finite element solutions based on Centroidal Voronoi Delaunay triangulations [14–18, 27] for the derivation of asymptotically exact a posteriori error estimations, and the use of localized Lloyd iterations [34] for efficient high quality meshing. Moreover, we show that these ideas can be seamlessly and systematically integrated into a successful and convergent adaptive finite element algorithm.

Let us first provide some brief discussions on several key components of AFEM and review some existing works. We note that given the large literature on the subject, our discussion is very limited and only some most relevant works to our approach are mentioned.

First, among the various a posteriori error estimation approaches, the residual-based and recovery-type methods have been widely accepted [1, 4, 36, 43, 45]. A particularly popular method is the ZZ-SPR approach, which is based on a local least squares fitting and has been widely used in numerical engineering practices, especially in commercial softwares, due to its robustness in effective a posteriori error estimates and its efficiency in computer implementation [45]. It is a common belief that the robustness of the Z-Z technique is rooted in its superconvergence property under structured or mildly structured meshes [4, 36, 43], which can be generated using many existing mesh generators [14, 15, 23, 41]. In [43], the effectiveness of the ZZ-SPR technique for linear triangular elements was established provided that the mesh satisfies the strong regularity or the quadrilateral parallelogram property. The construction of a triangular mesh with such a property and a given sizing specification has also been well documented. If such superconvergence properties hold for meshes in an adaptive procedure, one can then expect to get asymptotically exact a posteriori error estimators based on the superconvergent gradient recovery, which in turn leads to the convergence of the adaptive method. A series of works have been given by Bank et al. on recovery type a posteriori error estimates and improvement on mesh qualities. In [5], the mesh quality is improved using a posterior error estimator and in [6], the recovery type (by the global L2 projection) a posteriori error estimator was proved to be asymptotically exact on the improved mesh. Extensive numerical examples can be found in [7].

As for high quality two dimensional mesh generation, among many available techniques, the Centroidal Voronoi Tessellations (CVT) [13], whose generating points are also the mass centroids of the corresponding Voronoi regions with respect to a given density function, and their dual Centroidal Voronoi Delaunay Triangulations (CVDT) [14] have been developed for mesh generation and optimization with much success [14–18]. The construction of CVDT through the Lloyd iteration [34], which iteratively moves generators to the mass centres (of the Voronoi regions), provides effective reduction of the global distortion of element shape and sizing [18]. The converged CVDT has minimal distortion and shares good element quality with respect to the given sizing distribution. It possess mildly structured regularity which results in nice properties for superconvergent recovery [19, 21, 27]. Indeed, in [27], superconvergence was found for the finite element solution on a general two dimensional domain due to the nice quality of the CVDT mesh. While the use of CVDT in the AFEM context has been previously explored in [14, 28], none of those works have adopted the superconvergence based a posteriori error estimation. Motivated by the work in [27], we develop a convergent adaptive finite element method for two dimensional elliptic problems through a natural integration of the CVT based meshing and superconvergent gradient recovery based error estimation.

We now give a brief outline of our new method. Initially, a coarse CVT-based triangular mesh with either a uniform or a pre-determined sizing is constructed by performing the Lloyd iteration. Then, the iterative loops of finite element solution, error estimation and mesh refinement are executed. Three kinds of gradient recovery methods, namely, the weighted averaging, SPR and PPR techniques [24–26, 32, 36, 44] are tested. Based on the obtained error estimation, a new mesh sizing function is defined on each vertex by applying an error equal distribution principle proposed in [45]. The mesh sizing distribution is smoothed by performing gradation operated on edges [40]. As for the local refinement/coarsening required for making the current mesh consistent with the modified mesh sizing, a robust procedure proposed in [40] for surface remeshing is applied here. The mesh refined through local mesh operations needs to be improved further, with respect to the vertex distribution and the mesh topology, which is of paramount importance for the superconvergent gradient recovery. A localized and accelerated version of the popular Lloyd iteration [34] is developed in this work. The updated CVT-based triangular mesh is of high quality and can be readily used for the new loop of adaptation.

In the newly developed AFEM procedure described here, after each mesh *REFINE*, due to the nice properties of CVT-based optimization, the updated triangular mesh is of high quality which assures the superconvergence property of the recovered gradients and the asymptotical exactness of the a posteriori error estimate. Based on the equal distribution principle employed in the mesh sizing modification, the effectiveness of the error estimation leads to the convergence of the whole adaptation procedure. The convergence is verified through extensive numerical experiments.

The remainder of the paper is organized as follows: first in Section 2, we discuss finite element superconvergent gradient recovery based on the Centroidal Voronoi Delaunay meshing and a posteriori error estimation. In Section 3, the details of the adaptive finite element method are presented. In Section 4, several numerical experiments are described. Finally, conclusions and future working directions are given in Section 5.

2 CVT-based superconvergent gradient recovery and error estimation

Let Ω be a two dimensional bounded domain, we consider the following boundary value problem

$$\begin{cases} -\nabla\cdot(a\nabla u)=f, & \text{in } \Omega, \\ u=g, & \text{on } \partial\Omega, \end{cases} \tag{2.1}$$

where a, f and g are functions defined on $\overline{\Omega}$. For the case $g=0$, the weak formulation for the above model problem is: find $u\in H_0^1(\Omega)$, such that

$$\int_\Omega a\nabla u\nabla v=\int_\Omega fv$$

for all $v\in H_0^1(\Omega)$. The finite element method for Eq. (2.1) is to find $u_h\in S^h$, such that

$$\int_\Omega a\nabla u_h\nabla v=\int_\Omega fv, \qquad \forall v\in S^h, \tag{2.2}$$

where the linear finite element space S^h can be defined as

$$S^h=\Big\{v|v\in H_0^1(\Omega),\ v|_t\in P_1(t),\ \forall t\in T\Big\},$$

where T is a triangulation of Ω, P_1 denotes the linear function space, and h is the mesh parameter. The case of inhomogeneous boundary conditions can be considered similarly [9,11].

For effective and robust adaptation of the finite element solution procedure, it is required to derive a reliable error estimate in terms of the computed finite element solution u_h. There are many techniques for error estimations such as explicit estimator, hierarchical method, residual-type and recovery-type methods [1,2,35,44]. The residual based error estimators were first introduced in 1978 by Babuška-Rheinboldt [2] and have been studied by many others. Zienkiewicz-Zhu (Z-Z) introduced, in 1987, the first recovery based error estimator, then in 1992, the Superconvergent Patch Recovery (SPR) using local discrete least-squares fitting [4, 43, 45]. Further improvement can be found in [1, 26, 32, 33]. Recently, Zhang introduced the PPR technique which is also recovery based [36]. In this work, we apply the recovery-type technique to derive a posteriori error estimation. A few typical approaches are briefly reviewed in the next subsection.

2.1 Superconvergent gradient recovery and a posteriori error estimation

Let $\mathcal{N}_h$ be the set of mesh nodes. For a given vertex $z \in \mathcal{N}_h$, ω_z is used to denote the patch which consists of the triangles connecting z. Let G_h be a gradient recovery operator for the finite element solution u_h and $G_h u_h$ be the recovered gradient. To facilitate the computation, local coordinates are employed within each patch, and c_{τ_j} is defined as the barycenter of the triangle $\tau_j \subset \omega_z, j=1,2,\cdots,m$, where m is the number of triangles in the patch.

The simplest way to recover the gradient is by weighted averaging (WAV for short). The recovered gradient $G_h u_h$ at node z has the form of

$$G_h u_h(z) = \sum_{j=1}^{m} \frac{|\tau_j|}{|\omega_z|} \nabla(u_h^j), \tag{2.3}$$

which is a weighted linear combination of the gradients within each triangle of the element patch. $\nabla(u_h^j)$ denotes the gradient, $|\tau_j|$ is the weight and $|\omega_z| = \sum_{j=1}^{m} |\tau_j|$. The weights can be the areas of element, or other kind of quantities. A very popular choice is the so called ZZ-SPR technique. For a given vertex z, the ZZ Superpatch Recovery (ZZ-SPR) method assumes that the gradient function to be recovered is linear within the patch $\tilde{\omega}_z$. The gradient $\nabla(u_h^j)$ is sampled at the centroid c_{τ_j} of each element τ_j in the patch ω_z. The centroids and the gradients $\nabla(u_h^j), j=1,m$, are used to conduct least square fitting for the two linear gradient functions, i.e., the x- and y-component of the gradient. Special care is required for handling the boundary points. The readers are referred to [44,46] for the details of the recovery procedure. Different from the ZZ-SPR technique, the recently developed PPR method first applies least square fitting to reconstruct the function u_h as a quadratic function $p(z)$ within the patch ω_z. At least six mesh nodes connecting or around z (including z itself) are chosen and their finite element function values are utilized as the sampling values for the least square approximation. Similarly, special treatment is conducted for the boundary points. When the expression of $p(z)$ is obtained, the PPR-recovered gradient at z is defined to be $G_h u_h(z) = \nabla p(z)$, see [36] for details. In this paper, the ZZ-SPR technique is adopted for the gradient recovery, but the superconvergent properties of the CVDT meshes are shown to be valid for other recovery techniques as well.

Let $\{v_z : z \in \mathcal{N}_h\}$ be the Lagrange basis of S^h, then the recovered gradient $G_h u_h$ on $\bar{\Omega}$ can be defined to be

$$G_h u_h = \sum_{z \in \mathcal{N}_h} G_h u_h(z) v_z.$$

And the a posteriori error estimate can be conducted as

$$\eta_\Omega^2 = \sum_{\tau\in\mathcal{T}^h} \eta_\tau^2 = \|\nabla u_h - G_h u_h\|_{0,\Omega}^2, \tag{2.4}$$

where

$$\eta_\tau = \|\nabla u_h - G_h u_h\|_{0,\tau}$$

stands for the error estimate on each element τ. Asymptotic exactness of the error estimation can be obtained, provided that the recovered gradient $G_h u_h$ shares the superconvergent property [26, 32, 33, 44], which often requires certain topological and structural regularities of the finite element mesh possesses [43]. For instance, in [43], it was proved that η_Ω is asymptotically exact if the mesh is mildly structured (such as satisfying the $\mathcal{O}(h^{1+\alpha})(\alpha>0)$ parallelogram property), superconvergence results can be established for WAV, ZZ-SPR recovery and PPR. A natural question is how to generate a *superconvergent* mesh for a complicated domain, especially in the case of an adaptively updated nonuniform mesh sizing. We demonstrate here the CVT and CVDT based meshes can serve the purpose.

2.2 CVT-based high quality meshing for superconvergence

The centroidal Voronoi tessellation (CVT) and its wide applications have been studied in [13]. It provides optimal points placement with respect to a given density function as well as optimal spatial tessellation. With the density function properly related to a giving sizing field, its dual Centroidal Voronoi Delaunay triangulation (CVDT) results in a high-quality Delaunay mesh. Such techniques have been applied to isotropic mesh generation and optimization both in 2D and 3D [14–16,18]. Generalizations to anisotropic cases and surface quality mesh have also been made in [17]. We now recall some of the main concepts and properties of CVTs given in [13,18], and present the Lloyd method for the CVDT construction as an approach to optimize a Delaunay mesh [34].

2.2.1 Basic concepts and properties

Given a density function ρ defined on a region V, the *mass centroid* $\mathbf{z}^*$ of V is defined by

$$\mathbf{z}^* = \frac{\int_v \mathbf{y}\rho(\mathbf{y})d\mathbf{y}}{\int_v \rho(\mathbf{y})d\mathbf{y}}.$$

Given a set of points $\{\mathbf{z}_i\}_{i=1}^k$ in the domain Ω and a positive density function ρ defined on Ω, a Voronoi tessellation is a *Centroidal Voronoi Tessellation* (CVT) if $\mathbf{z}_i = \mathbf{z}_i^*$, $i = 1,\cdots,k$, i.e., the generators of the Voronoi regions V_i, $\mathbf{z}_i$, are themselves the mass centroids of those regions. The dual Delaunay triangulation is referred to as the *Centroidal Voronoi-Delaunay Triangulation* (CVDT).

For any tessellation $\{V_i\}_{i=1}^k$ of the domain Ω and a set of points $\{z_i\}_{i=1}^k$ (independent of $\{V_i\}_{i=1}^k$) in Ω, we define the following *cost* or *energy* functional:

$$F\big(\{V_i\}_{i=1}^k,\{z_i\}_{i=1}^k\big)=\sum_{i=1}^k\int_{V_i}\rho(x)\|x-z_i\|^2dx.$$

The standard CVTs along with their generators are critical points of this cost functional. The definitions of Constrained CVT (CCVT) and its dual constrained CVDT (CCVDT) can also be defined similarly; see [14] for details. Also, in [17], these concepts were generalized to anisotropic cases with a Riemannian metric and surface meshing.

CVT and CVDT's can be constructed by both probabilistic and deterministic methods [13, 14]. Here, we apply a deterministic algorithm based on the popular Lloyd's method [13, 14, 34], which is an iteration between constructing Voronoi tessellations and centroids. It enjoys the property that the functional F is monotonically decreasing throughout the iteration.

Given a bounded domain and a prescribed element sizing, suppose a Delaunay triangular mesh is constructed by a procedure that includes boundary discretization, constrained boundary Delaunay triangulation, interior points generation and Delaunay insertion of them, and also suppose that the constrained boundary Delaunay triangulation of the domain with respect to the sizing is provided [14, 15], the Lloyd iteration for the construction of CVT (and CVDT) can be briefly described as follows:

Algorithm 2.1. The Lloyd Iteration

1. Construct the Voronoi region for each of the interior points that are allowed to change their positions, and construct the mass center of the Voronoi region with a properly defined density function $\rho(p)$ derived from the sizing field $H(p)$ (with $\rho(p)=1/H(p)^{2+d}$ up to a constant scaling, where $d=2$ for two dimensions [14]).
2. Insert the computed mass centers into the constrained boundary Delaunay triangulation through a constrained Delaunay insertion procedure [23, 41].
3. Compute the difference $D=\sum_{i=1}^k\|P_i-P_{imc}\|^2$, $\{P_i\}$ is the set of interior points allowed to change, $\{P_{imc}\}$ is the set of corresponding computed mass centers. If D is less than a given tolerance, terminate; otherwise, return to Step 1.

The construction of CVDT (or CCVDT) through the above Lloyd iteration can be also viewed as a smoothing process of an initial mesh. The CVDT concept provides a good theoretical explanation to the effectiveness: by successively moving generators to the mass centers (of the Voronoi regions), the cost functional is reduced. Here, *smoothing* means both node-movement and node reconnection. As the density function is chosen according to the sizing function, the cost functional may be related to the distortion of the mesh shape and quality with respect to the mesh sizing. Thus, the process of iteratively constructing CVDTs, like the Lloyd's algorithm, leads to a reduction of the global distortion of element shape and sizing. The final CVDT would have the minimal distortion, and hence shares good element quality with respect to the sizing distribution [14, 15]. The optimized triangular mesh is almost equilateral for much of the domain, and the mesh satisfies the requirement of the so-called $\mathcal{O}(h^{1+\alpha})$ parallelogram property [43], see also [12] (pp. 285), as demonstrated numerically in the following subsection.

2.2.2 Numerical demonstration of superconvergent meshing

Superconvergent gradient recovery requires nice geometric properties of meshes, such as $\mathcal{O}(h^{1+\alpha})$ parallelogram property proposed in [12] for two dimensional geometry. Here, we introduce a parameter $\theta(h)$ to depict the geometric property of meshes

$$\theta(h) := \Big[\sum_{e\in\mathcal{E}} \big((\theta_{e1'} - \theta_{e1})^2 + (\theta_{e2'} - \theta_{e2})^2 \big) (S_\tau + S_{\tau'}) \Big]^{\frac{1}{2}},$$

where $\mathcal{E}$ is the set of interior edges in the triangulation $\mathcal{T}_h$. $\theta_{e1'}$, θ_{e1} and $\theta_{e2'}$, θ_{e2} are the alternate interior angles of the common side e of adjacent elements. S_τ and $S_{\tau'}$ denote the areas of the two neighboring elements, respectively (see Fig. 1). We say the triangulation $\mathcal{T}_h$ is α-superconvergent if $\theta(h) = \mathcal{O}(N^{-\alpha/2})$, with N being the total number of degrees of freedom (element nodes).

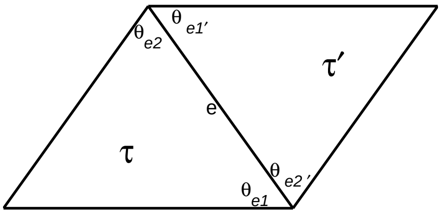

Figure 1: Alternate interior angles of the common side e of the neighboring elements τ, τ'.

To study the geometric properties of a mesh, the average element quality is also computed. Here, the element quality Q_τ of a triangle τ is defined as

$$Q_\tau = \frac{4\sqrt{3} S_\tau}{\sum_{i=1}^{3} (L_i)^2},$$

where $L_i (i = 1,2,3)$ denote the element edge lengths. The bigger the Q_τ is, the better the quality is. For an equilateral triangle τ, Q_τ is equal to 1. And the average quality of a triangular mesh $\mathcal{T}$ can be defined as $Q_{avg} = M^{-1} \sum_{i=1}^{M} Q_{\tau_i}$, where M is the number of elements.

Initially, CVT-based meshing and optimization are conducted for three domains with five scales of uniform mesh sizings, of which the coarsest scale meshes are shown in Fig. 2(a), (b), and (c) respectively. The mesh geometric statistics data involving average quality and the superconvergence parameters are included in Tables 1, 2, and 3 for each domain. For the three domains, all the meshes have average qualities up to 0.99 which

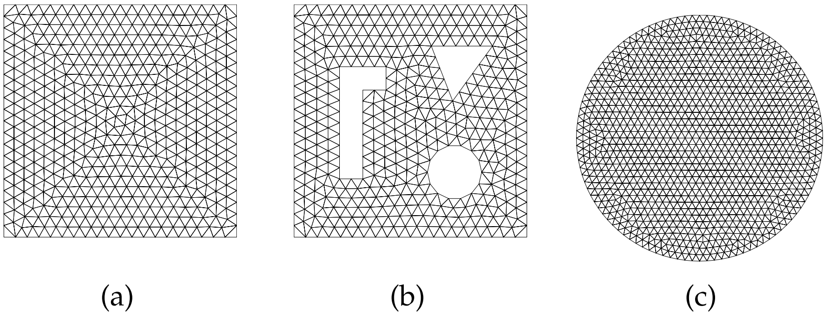

(a) (b) (c)

Figure 2: CVDT meshes of a domain with a complicated boundary (a) and a domain with three holes (b).

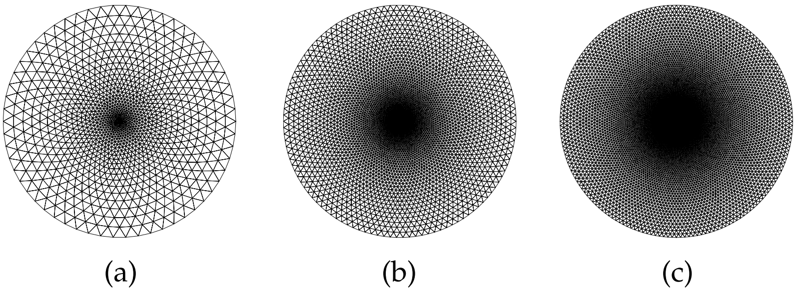

(a) (b) (c)

Figure 3: CVDT nonuniform meshes of a circular domain using sizing function $h=h_0=0.1\sqrt{x^2+y^2}+0.01$, $h=h_0/2$ and $h=h_0/4$ for (a), (b), (c) respectively.

demonstrate that the triangular meshes are almost equilateral, and accordingly the parameter α is about 0.5, corresponding to the domain shown in Figs. 2(a), (b), and (c) respectively. This shows that the meshes generated via CVT-based optimization are of nice parallelogram property. Moreover, it indicates that a better average element quality also leads to a better fit with the parallelogram property.

For CVT-meshing with non-uniform sizings, a unit disk is first meshed with refinement around its center, with the global mesh sizing function defined as $h=h_0(x,y)=0.1\sqrt{x^2+y^2}+0.01$. Then, h is reduced to be $h_0/2.0$, $h_0/3.0$ and so on for global refinement. Three CVT-meshes are shown in Figs. 3(a), (b), and (c) respectively and the parallelogram property parameters are contained in Table 4 from which it is clear that superconvergent meshes are constructed.

Table 1: Mesh data including the mesh sizing, element average quality and the order of convergence α in the case where the mesh is shown in Fig. 2(a).

Sizing h	0.05	0.025	0.0125	0.009	0.00625
Q_{avg}	0.991	0.996	0.998	0.999	0.999
N	499	1923	7566	14510	29960
$\theta(h)$	0.298	0.233	0.133	0.122	0.105
α	—	0.535	0.498	0.493	0.498

Table 2: Mesh data including the mesh sizing, element average quality and the order of convergence α in the case where the mesh is shown in Fig. 2(b).

Sizing h	0.05	0.025	0.015	0.009	0.0065
Q_{avg}	0.985	0.992	0.995	0.997	0.998
N	450	1703	4619	12632	24074
$\theta(h)$	0.320	0.241	0.194	0.154	0.131
α	—	0.42	0.43	0.46	0.50

Table 3: Mesh data including the mesh sizing, element average quality and the order of convergence α in the case where the mesh is shown in Fig. 2(c).

Sizing h	0.08	0.06	0.04	0.02	0.01
Q_{avg}	0.989	0.993	0.996	0.998	0.999
N	631	1085	2375	9267	23503
$\theta(h)$	0.539	0.402	0.326	0.226	0.160
α	—	1.09	0.534	0.536	0.503

Table 4: Mesh data including the total mesh nodes, element average quality and the order of convergence α in the case where the mesh is nonuniform in Fig. 3.

N	1189	4678	10485	18550	23503
Q_{avg}	0.988	0.994	0.995	0.995	0.995
$\theta(h)$	0.378	0.237	0.190	0.163	0.150
α	—	0.678	0.551	0.536	0.688

Table 5: Mesh data including the total mesh nodes, element average quality Q_{avg} and $Q_{avg(loc)}$ (the element average quality within the red circular domain) for the nonuniform mesh in Fig. 4.

N	412	1375	2349	3288
Q_{avg}	0.980	0.991	0.995	0.994
$Q_{avg(loc)}$	0.980	0.988	0.991	0.991

Next, the unit disk is chosen again and the mesh sizing $h(x,y)$ is defined in the following way. The sizings for the boundary is fixed to be $hb=0.1$, the sizing for the center is fixed to be $hc=0.1$ first, and for the other parts of the domain, linear interpolation between hb and hc is applied. The first CVT-mesh is shown in Fig. 4(a). Then, hc is reduced to be 0.05, 0.025 and so on, and linear interpolation is again conducted for mesh sizings. A sequence of CVT-meshes are generated and they are shown in Figs. 4(b), (c), and (d). High-quality meshes are constructed which is demonstrated by the local views of the mesh around the disk center shown in Fig. 5 and it is also clearly shown by the average qualities contained in Table 5. This substantiates that CVT-based mesh optimization technique is suitable for superconvergent gradient recovery, which shall be further demonstrated in the following.

Three complicated domains are chosen as examples for CVT-based meshing and

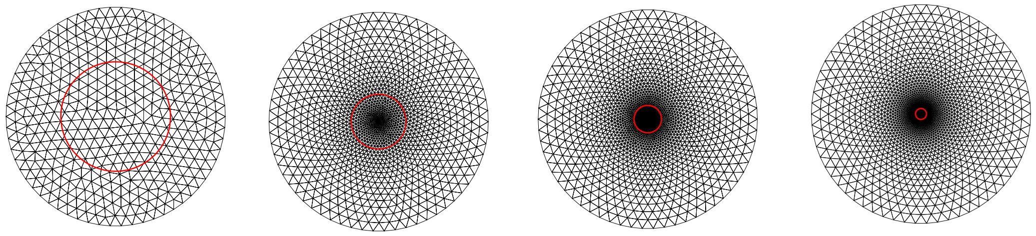
(a) (b) (c) (d)

Figure 4: Nonuniform CVDT meshes of the unit disk (the radii of the red circles are 1/2, 1/4, 1/8, and 1/16, respectively).

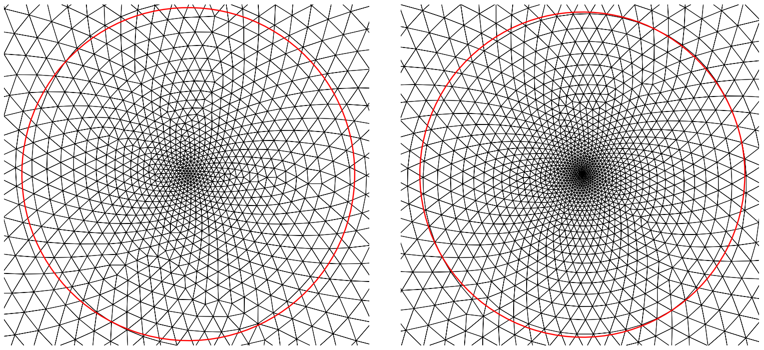
(a) (b)

Figure 5: Local views of the mesh near the singular point in Fig. 4(c) and (d).

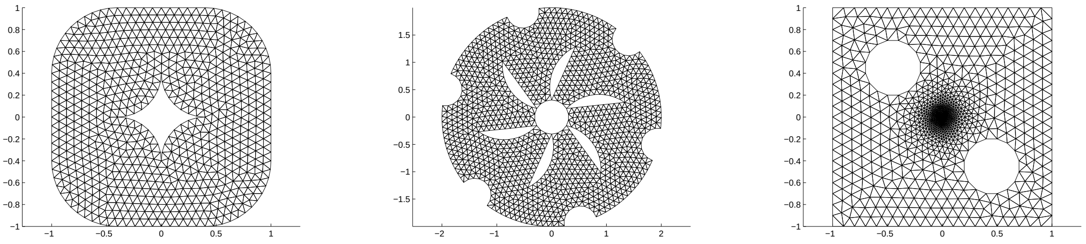

(a) (b) (c)

Figure 6: CVDT meshes for superconvergent gradient recovery.

among which, two domains are meshed with uniform sizings of four different scales (levels) with the third being meshed with a point refinement, as illustrated in the Figs. 6(a), (b), and (c), respectively. Eq. (2.2) (with $a=1$) is solved on these meshes by finite element method with conforming linear elements. Also, gradient recovery is conducted via the WAV, ZZ-SPR and PPR methods.

For a two dimensional problem, the standard optimal convergence rate for linear finite elements is: $||\nabla(u-u_h)||_{L_2(\Omega)} \leq CN^{-1/2}$. And the recovered gradient $G_h u_h$ is said

Table 6: Mesh data including the mesh quality, error estimate $\|\cdot\| = \|G_h u_h - \nabla u\|_{L^2(\Omega)}$ and the order of convergence for the recovered gradients for the mesh shown in Fig. 6(a) and the exact solution $u = e^{(x^2+y^2)}$.

Sizing h	0.16	0.08	0.04	0.02
Q_{avg}	0.974	0.981	0.988	0.992
N	190	739	2829	11051
$\|\cdot\|_{WAV}$	2.584e-1	8.024e-2	2.372e-2	6.617e-3
CR_{WAV}	—	1.722	1.816	1.874
$\|\cdot\|_{PPR}$	2.418e-1	7.689e-2	2.244e-2	6.064e-3
CR_{PPR}	—	1.687	1.835	1.920
$\|\cdot\|_{ZZ}$	2.371e-1	7.598e-2	2.198e-2	5.919e-3
CR_{ZZ}	—	1.676	1.848	1.926

Table 7: Mesh data including the mesh quality, error estimate $\|\cdot\| = \|G_h u_h - \nabla u\|_{L^2(\Omega)}$ and the order of convergence for the recovered gradients for the mesh shown in Fig. 6(b) and the exact solution $u = \sin(6x)\sin(6y)$.

Sizing h	0.2	0.1	0.05	0.025
Q_{avg}	0.967	0.981	0.988	0.991
N	366	1325	5099	19898
$\|\cdot\|_{WAV}$	4.578	1.648	4.517e-1	1.193e-1
CR_{WAV}	—	1.648	1.920	1.956
$\|\cdot\|_{PPR}$	4.703	1.636	4.481e-1	1.167e-1
CR_{PPR}	—	1.642	1.922	1.979
$\|\cdot\|_{ZZ}$	4.730	1.641	4.487e-1	1.164e-1
CR_{ZZ}	—	1.646	1.924	1.982

to be superconvergent in the sense that $||\nabla u - G_h u_h||_{L_2(\Omega)} \leq CN^{-1/2-\rho}$, where $\rho > 0$ is a constant and $G_h : P_1 \times P_1$ is the recovery operator. Then, the convergence rate CR with respect to the norm $\|\cdot\|$ at the refinement level l is computed by

$$CR = \frac{2\log\left(\|e_l\|/\|e_{l-1}\|\right)}{\log\left(N_{l-1}/N_l\right)}, \tag{2.5}$$

where N_l and e_l are the number of degrees of freedom and $\nabla u - G_h u_h$ in the l^{th} refinement level, respectively.

For the computed finite element solutions, several kinds of data are computed and they include the *mesh size h*, the average mesh quality Q_{avg}, the number of the nodal freedoms N, the error estimate $\|G_h u_h - \nabla u\|$ of the recovered gradient, and the CR of the order of convergence determined by the expression (2.5). Table 6 and Table 7 contain the data corresponding to the use of WAV, PPR and ZZ-SPR respectively, which clearly demonstrate that superconvergence property are obtained. Also, it is found that the three recovery methods are comparable on the constructed CVDT meshes. Table 8 contains the data corresponding to the case where the solution is singular at the center of the domain and the gradient recovery is conducted only by ZZ-SPR. It further demonstrates that tri-

Table 8: Mesh data including the number of nodal freedoms N, the mesh quality, error estimate $\|\cdot\| = \|G_h u_h - \nabla u\|_{L^2(\Omega)}$ and the order of convergence for the recovered gradients for the mesh shown in Fig. 6(c) and the exact solution $u = 1.0/(x^2+y^2+0.01)$. Only ZZ-SPR is shown here.

N	Q_{avg}	$\|\cdot\|$	CR_{ZZ}
463	0.985	67.403	—
980	0.979	2.727	8.607
1557	0.979	1.831	1.726
4204	0.980	0.643	2.111
9603	0.981	0.279	2.023
14754	0.982	0.181	2.016

angular meshes with nice parallelogram property can be generated based on CVT optimization and this leads to guaranteed superconvergent gradient recovery, which would be exploited for the development of convergent adaptive finite element method in the following sections.

3 Convergent adaptive FEM for elliptic problems

In the AFEM considered here that consists of the loops of

$$\text{SOLVE} \rightarrow \text{ERROR ESTIMATE} \rightarrow \text{REFINE/COARSEN},$$

the procedure SOLVE is carried out to solve the elliptic PDE, say Eq. (2.2), for the finite element solution on the current mesh. With the computed finite element solution, the superconvergent gradient recovery using ZZ-SPR is performed for the a posteriori error estimation. Then, based on the principle of equal error distribution, the mesh sizing of each vertex is modified. The procedure REFINE/COARSEN modifies the current triangular mesh by inserting points or contracting edges iteratively so that the refined mesh is consistent with the new mesh sizing distribution. The refined mesh is further optimized via a modified Lloyd iteration to construct an almost equilateral CVDT mesh. The procedures SOLVE and ERROR ESTIMATE were discussed before in Section 2, and mesh sizing modification and remeshing will be discussed next, followed by a summary of the whole adaptive finite element algorithm.

3.1 Mesh sizing modification

The sizing function defined on each vertex is computed as the average length of the mesh edges connecting the vertex. Based on the principle of equal distribution of errors over each triangle, the sizing function of the current triangular mesh is modified in the method proposed in [46], where the readers are referred to for details.

The average length of the edges of a triangle is defined as the sizing of the triangle denoted by h_{old} in the current mesh, based on which a new sizing denoted by h_{new} can be derived. First, we define the *Permissable Error* E_p by

$$E_p = \mu \sqrt{\frac{\|u_h\|^2_{E(\Omega)} + ||e_h||^2_{L^2(\Omega)}}{M}},$$

where M is the number of elements in the mesh and μ is a pre-assigned positive constant usually with a value less than 1. A smaller μ leads to a smaller permissable error which requires a finer mesh. Here, $\|u_h\|^2_{E(\Omega)}$ is the energy norm of the finite solution u_h over the domain, and e_h is defined as $G_h u_h - \nabla u_h$. Then,

$$h_{new} = \frac{h_{old}}{E_\tau / E_p},$$

where E_τ is the error on each element τ in the form of $||G_h u_h - \nabla u_h||_{L_2(\tau)}$ and E_{melm} is the maximum of E_τ over all elements. The sizing of each vertex is defined as the average of the new sizings of the elements sharing the vertex.

The mesh sizing modification will be followed by sizing gradation which is realized by applying the H-correction procedure proposed in [40], which will reduce the magnitude of ratio of neighboring edge lengths and smooth the sizing distribution as a result. The smoothed sizing function will be used for the refinement or coarsening of the current mesh next.

3.2 Remeshing through edge splitting/contraction

The refinement of a given triangular mesh is composed of several local mesh operations involving edge splitting/contraction, edge swapping and point smoothing [40]. Edge splitting and contraction are based on the computation of normalized edge lengths [40], which is utilized as a criterion for the refinement or coarsening of the given edge. Usually, the value $C_s = \sqrt{2}$ is assigned to the splitting parameter, and the value $C_c = 1/\sqrt{2}$ is set to be the coarsening parameter. If an edge has a normalized length larger than C_s then a splitting operation is performed, while a contraction is applied if the edge length is less than C_c. We outline next the four elementary mesh modification operators, which is followed by a complete description of the mesh refinement and coarsening procedure. The readers are referred to [40] for details.

Edge Splitting. For any edge which has a normalized edge length larger than the given splitting criterion C_s, the midpoint of the edge is introduced as a new point and the edge is then halved with the two triangles adjacent to the edge being replaced by four new triangles.

Edge Contraction. When the normalized edge length of an edge is less than the collapse criterion C_c, the edge will be contracted in the way that either the two end points are merged into their midpoint or one of them is remove while keeping the other, which is illustrated Fig. 7. The merging technique shown in Fig. 7(b) is applied in this paper.

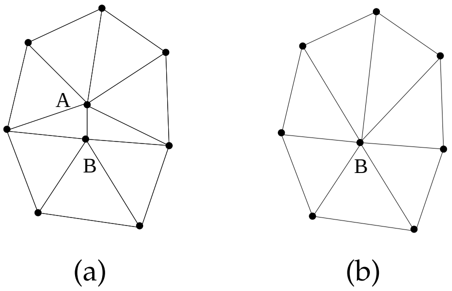

Figure 7: Two edge contraction schemes can be used: (a) AB is to be contracted; (b) B is chosen to be kept unchanged.

Edge Swapping. Given a non-boundary edge, swapping is allowed if the quad formed by the two adjacent triangles is a convex polygon. Let triangles K_1 and K_2 share a common edge e, and p_1, p_2 be the vertices of the triangles K_1 and K_2, which are opposite to the edge e. If p_1 is enclosed in the circumscribed triangle K_2 or equivalently p_2 is enclosed in the circumscribed triangle K_1, then edge swapping is performed through the replacement e by p_1p_2, of which the objective is to make the new edge satisfy the Delaunay property locally and also globally due to the Delaunay lemma [23]. In the two dimensional setting, the Delaunay property refers to that the interior of the open disc circumscribing a triangle K encloses no other vertex.

Point Smoothing. Point relocation or smoothing, modifies the position of a vertex without changing the topology of the triangles meeting at the vertex. The objective is to seek an optimal position on the mesh for the vertex, in the sense that any alternative configuration should have better quality, according to criterion such as minimal angle, shape quality, size conformity or others. Here, only the element shape quality is considered and various smoothing methods can be used [40].

Refinement/Coarsening Procedure. The refinement/coarsening procedure modifies, iteratively, an existing triangulation through edge splitting or contraction. The objective is to ensure that elements are in better conformity with the size distribution. Edge lengths computed (or normalized) with respect to vertex sizing function are compared with the given splitting parameter C_s and contraction parameter C_c. After the edge splitting and contraction, the triangulation is finally enhanced via a combination of edge swapping, point smoothing, node connectivity optimization. The combined application of these postprocessing techniques is found to be very effective in improving the regularity and smoothness of the mesh, which will function as a nice initialization for the following CVT-based optimization.

3.3 Localized Delaunay insertion for CVT-based mesh optimization

The convergence characteristics of the Lloyd iteration was investigated in [16] and [17]. The most effective part of the Lloyd iteration is the first few steps which reduces the convergence error and modify the mesh significantly. After that, the mesh changes very slowly.

In the Lloyd iteration, the total computation time equals to the number of iterations multiplied by the time for the calculation of the mass centers plus their Delaunay insertion. The mass center computation takes far less time than the Delaunay insertion. And in each Lloyd iteration, all the computed mass centers are inserted into the constrained boundary Delaunay triangular mesh in the Delaunay insertion kernel [14, 15] whatever the difference between an interior point and its corresponding mass center is. The original uniform treatment of Delaunay insertion of the mass centers does not fit well with the convergence characteristics of the Lloyd iteration. Hence, the Delaunay insertion should be modified and the new algorithm goes as follows.

Algorithm 3.1. (Modified Delaunay Insertion)

Given a Delaunay mesh and the computed mass centers for its interior points.

1. For each interior point, perform the following loop:
2. Replace the point with its corresponding mass center and check the validity of the Ball of the new interior point, defined as the union of all its connecting triangles, by computing all the signed areas of the connected triangles. If all such areas are positive, the check is passed; otherwise, the midpoint of the interior point and the mass center is used as a replacement and the check is continued recursively until termination.
3. Check the connecting edges of the new point and perform appropriate edges swapping on them to maintain their Delaunay property.
4. Perform the Lawson-swapping of edges recursively for the edges of the connecting triangles that are opposite to the new point, until the Delaunay property is satisfied for all triangles.

Fig. 8 depicts the complete procedure of the above modified Delaunay insertion of an updated interior point (i.e., the mass center), based on which the original Lloyd iteration is modified in the following manner:

Algorithm 3.2. (Modified Lloyd Iteration)

Given a Delaunay triangular mesh and its interior vertices.

1. Construct the Voronoi region for each of the interior points that are allowed to change their positions, and construct the mass center of the Voronoi region with a properly defined density function $\rho(p)$ derived from the sizing field $H(p)$ (here, $\rho(p)=1/H(p)^4$ up to a constant scaling).
2. Insert the computed mass centers into the current Delaunay triangulation through the Modified Delaunay insertion procedure presented in Algorithm 2.
3. Compute the difference $D=\sum_{i=1}^{k}\|P_i-P_{imc}\|^2$, where $\{P_i\}$ is the set of interior points allowed to change, and $\{P_{imc}\}$ is the set of corresponding computed mass center. If D is less than a given tolerance, terminate; otherwise, return to Step 1.

The above modified Lloyd iteration has two properties. One is that during the Lloyd iteration, more interior points can be replaced by their updated mass centers without

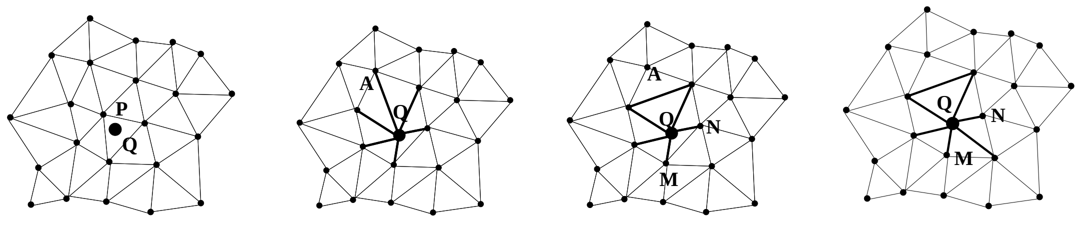

(a) (b) (c) (d)

Figure 8: Modified Delaunay insertion of an updated interior point by replacement and edges swapping: (a) Q is to be inserted and to replace P; (b) replace P; (c) neighboring edges swapping: AQ is swapped; (d) recursive Lawson-type edge swapping: MN is swapped.

conducting edge swapping in order to keep the Delaunay property. It reduces the computation in each Lloyd iteration to the mass center computation, which speeds up the Lloyd iteration significantly. The other is that in the above procedure, it is no longer necessary to construct and store a constrained boundary triangular mesh as in the previous works [14, 15, 17], which makes it possible to optimize any initial Delaunay triangular mesh in the modified Lloyd iteration. These two properties are essential to the development of the following algorithm for adaptive finite element method based on CVT.

3.4 Adaptive finite element method based on CVT

Let $\{z_i\}_{i=1}^{k^{(l)}}$ denote the set of points of the l-th level triangulation $M_h^{(l)}$ and $u_h^{(l)}$ is the corresponding finite element solution on $M_h^{(l)}$. The following summarizes the flow chart of the adaptive finite element method based on CVT.

Algorithm 3.3. (Adaptive FEM based on CVT)

Let Ω denote the given domain, $L_{\max}$ is the allowable maximal levels of mesh refinements, $N_{\max}>0$ is the allowable maximal number of mesh vertices, and $\delta := \left(|||u_h^{(l)} - u_h^{(l-1)}|||_E\right)/|||u_h^{(l)}|||_E$ denotes the relative difference of two consecutive finite element solutions in the energy norm.

1. Initialization: set $l=0$ and generate an initial coarse triangulation $M_h^{(0)}$ of Ω. $n^{(0)}$ denotes the number of vertices of $M_h^{(0)}$. Solve Eq. (2.2) by finite element method (FEM) on $M_h^{(0)}$.
2. Conduct gradient recovery in ZZ-SPR technique and calculate the error estimator η_τ for each element $\tau \in M_h^{(l)}$, and compute the new sizing h_{new} of each point followed by gradation.
3. Refinement/Coarsening: Compute the normal lengthes of all the edges on $M_h^{(l)}$, perform splitting/contraction edge and other operation involving edge swapping, smoothing and combined optimization.
4. CVT-based Optimization: apply Algorithm 3 to optimize $M_h^{(l)}$ and obtain $M_h^{(l+1)}$.
5. Solve the Eq. (2.2) by FEM on $M_h^{(l+1)}$. If $l > L_{\max}$, or $n^{(l)} > N_{\max}$, or δ is less than the given criterion, terminate; otherwise, go to Step 2.

4 Numerical experiments

In this section, the proposed CVT-based finite element method will be applied to the solution of Eq. (2.2). To demonstrate the generality and versatility of the proposed method, five experiments are conducted on different spatial domains that possess various geometric features; in addition, the exact solutions are pre-determined in all the experiments and for several instances, they contain different forms of singularities that are frequently encountered in practical applications. In Fig. 9, the domains used for Experiments 1 to 4 are shown, while the last experiment is performed on a square $\Omega=[-1,1]^2$. Statistics data related to the finite element mesh, solution and error estimation are presented for each experiment. The collected data include degree of freedoms N, average mesh quality Q_{avg}, permissible error E_p, maximal element error E_{melm}, the L^2 norm of the error $\|u-u_h\|$, the energy norm $|||u_h-u|||$, and another important parameter effectiveness index Ψ, which is defined as

$$\Psi:=\frac{\|a^{-\frac{1}{2}}(G_hu_h-a\nabla u_h)\|_0}{\|a^{\frac{1}{2}}(\nabla u-\nabla u_h)\|_0}.$$

In the following Experiments 1 to 4, $a=1$, so the exact gradient is to be recovered. For the very last experiment, a represents a discontinuous coefficient, so G_hu_h approximately recovers the flux.

Experiment 1: With a smooth exact solution. The first experiment is to solve Eq. (2.2) with $a=1.0$ on a complicated domain denoted by Ω which is shown in Fig. 9(a), and the exact solution is $u=x^2y^2$. The functions f and g are determined accordingly. The proposed CVT-based adaptive finite element method is applied to obtain a convergent solution.

The adaptive meshes are shown in Fig. 10, where the initial CVDT mesh and three other meshes corresponding to the 2nd, 3rd and 5th level of adaptive refinement are shown. The mesh is refined around the four corners in a modest manner, which is in good consistence with the characteristics of the solution. The finite element solution u_h on the final adaptive mesh (5th level) is presented in Fig. 11(a). The error distributions corresponding to the 2nd, 3rd and 5th adaptive meshes are shown in Figs. 11(b), (c), and (d) respectively, where it can be clearly seen that the error is almost equally distributed on the elements. This can also be well observed from the experimental data contained in Table 9. The maximal element error is $4.263e-5$ which is only two times of the permissible

Table 9: Statistics of the mesh, finite element solution and error of the Experiment 1 where the exact solution $u=x^2y^2$.

level	N	Q_{avg}	Ψ	E_p	Emelm	$\|u-u_h\|$	$\|\|\|u_h-u\|\|\|$
0	208	0.953	1.061	—	2.130e-3	1.795e-4	1.290e-2
2	1318	0.964	1.011	1.466e-4	2.267e-4	3.386e-5	4.114e-3
3	2495	0.972	1.006	7.507e-5	1.166e-4	1.849e-5	2.898e-3
5	5681	0.976	1.003	2.726e-5	4.263e-5	6.450e-6	1.862e-3

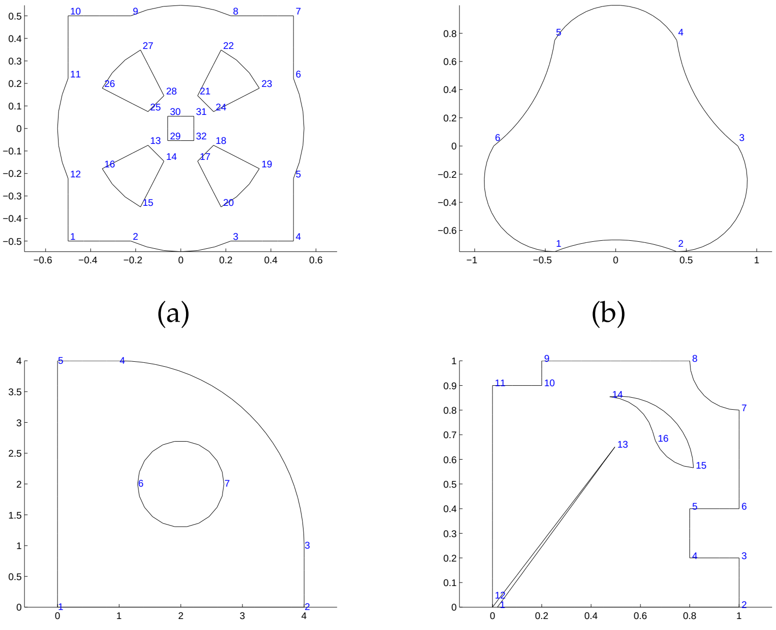

(a) (b)

(c) (d)

Figure 9: (a) A domain with several holes for the Experiment 1; (b) a curved domain for Experiment 2; (c) a domain for the Experiment 3 and (d) a concave domain with cracks for Experiment 4.

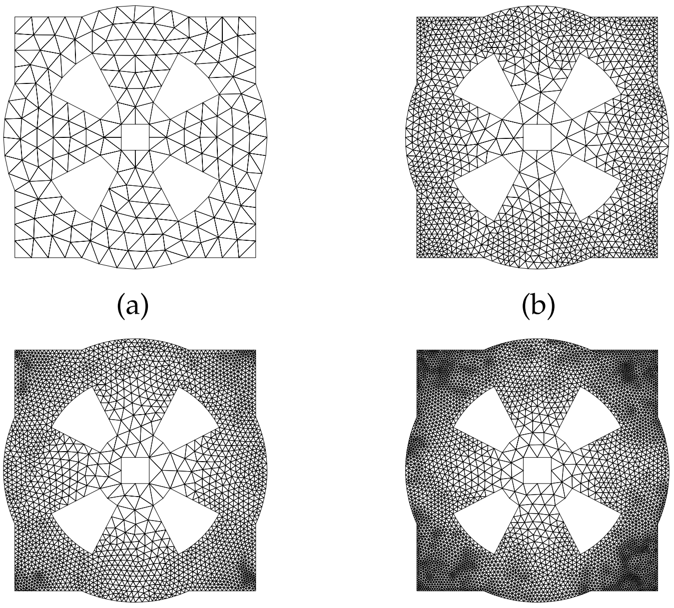

(a) (b)

(c) (d)

Figure 10: Adaptive CVDT meshes for the Experiment 1: (a) initial one; (b), (c), and (d) after 2, 3 and 5 refinements.

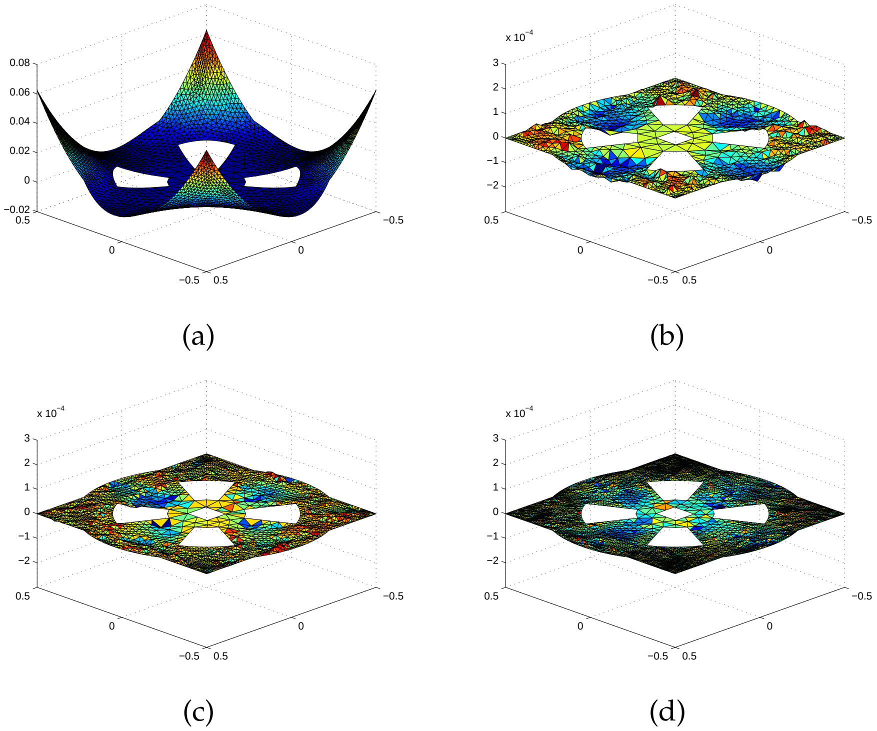

(a) (b) (c) (d)

Figure 11: Finite element solution and error distribution for the Experiment 1: (a) u_h on the fifth adaptive CVDT mesh; (b), (c), and (d) e_h corresponding to the adaptive CVDT mesh after 2, 3, 5 refinements, respectively.

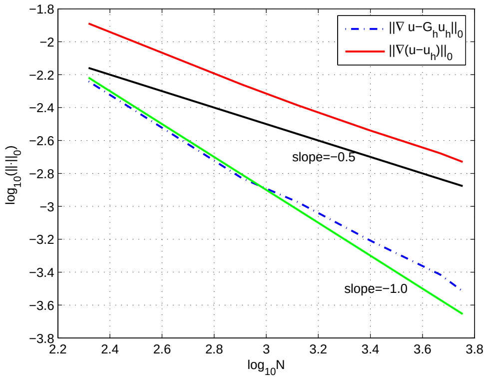

Figure 12: Quasi-optimality of the convergence rate of the adaptive FE procedure for the Experiment 1, where optimal decay is indicated by the line of slope -0.5.

error $2.726e-5$ on the final adaptive mesh. The effectiveness of the adaptive procedure can be further demonstrated by other statistics data in Table 9. The averaging mesh quality Q_{avg} of each mesh is up to 0.970, which leads to very good effectiveness indices. On all meshes, Ψ is very close to 1.0 and the fifth Ψ is up to 1.003, which shows that the a posteriori error estimation is asymptotically exact. The exactness results in the convergence of the whole adaptation procedure, which is further demonstrated in Fig. 12. From the dotted line, which is used to relate the error energy norm to the total degree of freedoms, it can be concluded that quasi-optimal convergence is achieved [10,28], compared with optimal convergence which is shown by the straight line with slope 0.5 contained in Fig. 12. This means that $|||u-u_h|||_\Omega = CN^{-1/2}$ is valid asymptotically and the superconvergence property of $\|a^{-1/2}(G_h u_h - a\nabla u)\|_0$ is also obtained.

Experiment 2: With three point singularities. In this experiment, the same PDE as in Experiment 1 is solved, with its domain Ω shown in Fig. 9(b). The exact solution u assumes the following form:

$$u(x,y) = \frac{1.0}{x^2+(y-0.5)^2+0.01} + \frac{1.0}{(x+0.4330)^2+(y+0.25)^2+0.01} + \frac{1.0}{(x-0.4330)^2+(y+0.25)^2+0.01},$$

which reaches its maximal values at three points (0,0.5), (-0.4330,-0.250) and (0.4330,-0.250), but decreases rapidly away from these maximums and thus has large gradients close to the three points.

Applying the CVT-based adaptive FEM method, in total 11 adaptive meshes are generated for the convergence of the whole procedure. Four meshes at different refinement level are chosen and shown in Fig. 13, which clearly shows the successive refinement

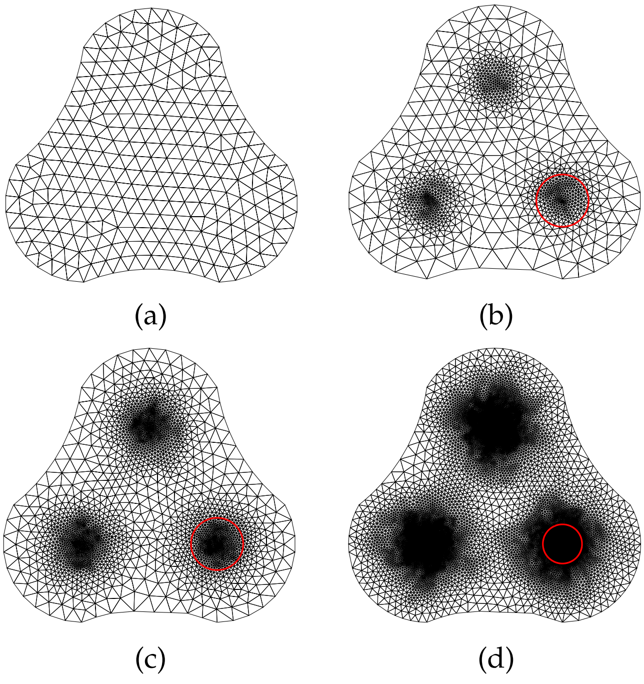
(a) (b) (c) (d)

Figure 13: Adaptive CVDT meshes for the Experiment 2: (a) initial one; (b), (c), and (d) after 4, 8 and 11 refinements.

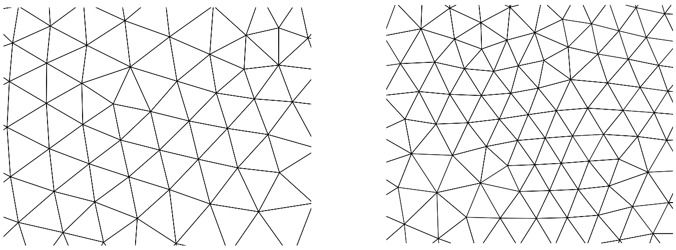

(a) (b)

Figure 14: Adaptive CVDT meshes for the Experiment 2: (a) the local view near the singularity point at the refinement level 8; (b) the local view near the singularity point at the refinement level 11.

around the three singular points. Also, the CVT-based optimized meshes assume very high qualities, which can be well demonstrated by the data contained in Table 10. The average mesh quality is up to 0.98 in the final mesh and all are above 0.971. To further demonstrate the high quality of the adaptive meshes, local views of the mesh around the singular area is shown in Fig. 14 and the quality data of the local meshes are contained in Table 11. From the local views and the quality data, it can be drawn that high quality adaptive meshes are generated for superconvergent gradient recovery.

Table 10: Statistics of the mesh, finite element solution and error of the Experiment 2 with three point singularities.

level	N	Q_{avg}	Ψ	E_p	E_{melm}	$\Vert u-u_h\Vert$	$\vert\vert\vert u_h-u\vert\vert\vert$
0	282	0.982	0.562	—	22.320	4.915	102.0
4	1206	0.971	1.020	0.7712	1.3210	0.2990	26.9920
8	3047	0.976	1.009	0.2606	0.4155	0.1196	16.3318
11	14176	0.980	1.001	0.0758	0.1148	0.02916	7.7176

Table 11: Mesh data including the number of mesh nodes, element average quality Q_{avg} and $Q_{avg(loc)}$ (the element average quality within the red circular domain) for the Experiment 2 (see Fig. 13).

Level	N	Q_{avg}	$Q_{avg(loc)}$	*Level*	N	Q_{avg}	$Q_{avg(loc)}$
0	282	0.982	0.985	6	2019	0.970	0.980
1	636	0.957	0.961	7	2952	0.974	0.980
2	728	0.965	0.973	8	3047	0.976	0.981
3	909	0.967	0.977	9	5260	0.975	0.980
4	1206	0.971	0.979	10	8675	0.976	0.981
5	1747	0.973	0.979	11	14176	0.980	0.981

As in the Experiment 1, the nice quality of the mesh leads to the superconvergence property even when the simplest method WAV is applied. And the superconvergent gradient recovery results in an asymptotical exactness in the error estimation which can be proved numerically from the effectiveness index Ψ values contained in Table 10. Accordingly, the max element error is very close to the permissible error E_p. It shows that

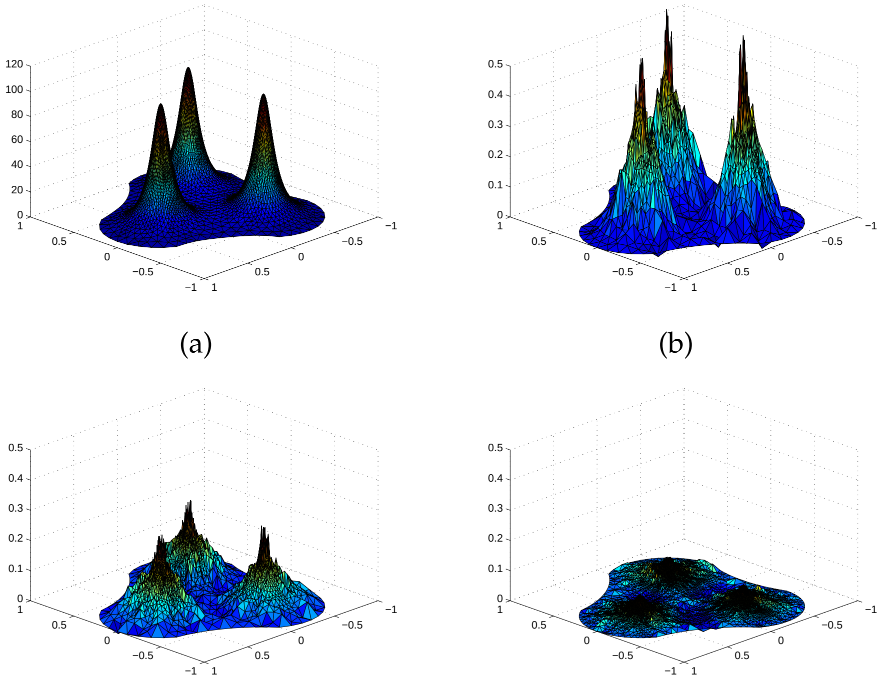

(a) (b)

(c) (d)

Figure 15: Finite element solution and error distribution for the Experiment 2: (a) u_h on the 11th adaptive CVDT mesh; (b), (c), and (d) e_h corresponding to the adaptive CVDT mesh after 4, 8, 11 refinements, respectively.

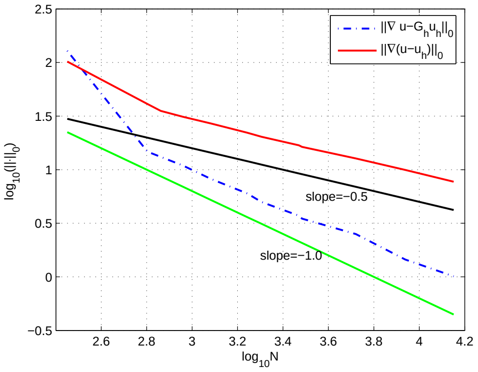

Figure 16: Quasi-optimality of the convergence rate of the adaptive FE procedure for the Experiment 2, where optimal decay is indicated by the line of slope -0.5.

the element errors are asymptotically equal-distributed, which can also be clearly seen from Fig. 15. Moreover, the adaptation procedure achieves quasi-optimality in convergence order, which is well demonstrated in Fig. 16 and the superconvergence property of $\|a^{-1/2}(G_hu_h - a\nabla u)\|_0$ is also obtained.

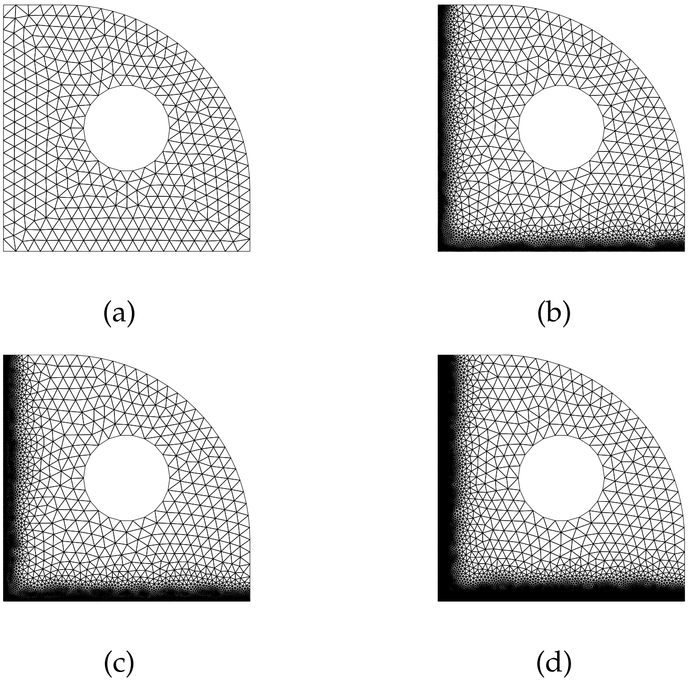

Figure 17: Adaptive CVDT meshes for the Experiment 3: (a) initial one; (b), (c), and (d) after 2, 5 and 8 refinements.

Experiment 3: With layer singularity. To test the capability of the adaptive FEM method to handle boundary layer singularities, the same equation is used, but with its exact solution u assuming the form of

$$u(x,y)=\frac{1.0}{x^2+0.01}+\frac{1.0}{y^2+0.01},$$

which has strong singularities occurring on the boundary $x=0$ and $y=0$.

The domain is shown in Fig. 9(c), the adaptive meshes are shown in Fig. 17, the statistics are included in Table 12. Both the mesh refinement and the data demonstrate that the CVT-based meshing and superconvergent gradient recovery lead to a very effective convergent finite element adaptation procedure. This can further be substantiated by the error distributions illustrated in Fig. 18 and the achieved asymptotical quasi-

Table 12: Statistics of the mesh, finite element solution and error of the Experiment 3 with layer singularities.

level	N	Q_{avg}	Ψ	E_p	E_{melm}	$\|u_h-u\|$	$\|\|u-u_h\|\|$
0	407	0.982	0.95	—	24.29	33.050	221.4
2	4125	0.967	1.010	1.153	1.801	0.4955	53.11
5	7782	0.974	1.032	0.4156	0.6877	0.2320	34.60
8	22303	0.980	1.010	0.1413	0.2087	0.09463	19.47

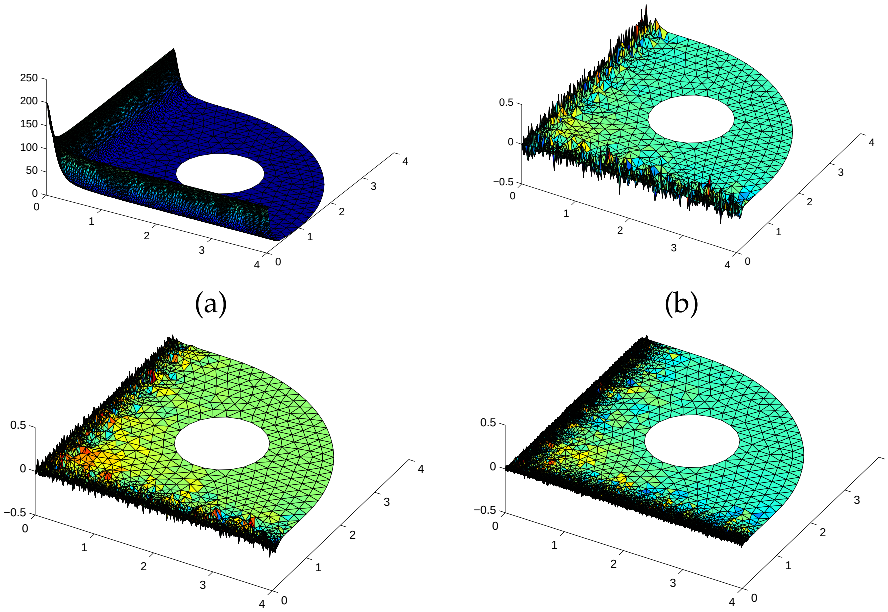

(a) (b)

(c) (d)

Figure 18: Finite element solution and error distribution for the Experiment 2: (a) u_h on the 8th adaptive CVDT mesh; (b), (c), and (d) e_h corresponding to the adaptive CVDT mesh after 2, 5, 8 refinements, respectively.

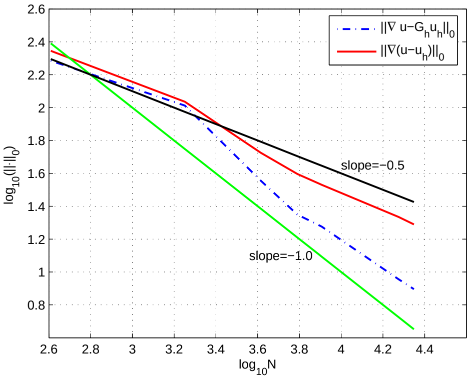

Figure 19: Quasi-optimality of the convergence rate of the adaptive FE procedure for the Experiment 3, where optimal decay is indicated by the line of slope -0.5.

optimality of the convergence order demonstrated in Fig. 19. The recovered energy error $\big(\|a^{-1/2}(G_h u_h - a\nabla u)\|_0\big)$ is given by the dotted line which also demonstrates the superconvergence property.

Experiment 4: Concave geometry with crack and corners. In order to test the robustness and the capability of the method to deal with complicated geometries, a concave domain with a crack and many corners is used in this experiment, see Fig. 9(d). Eq. (2.2)

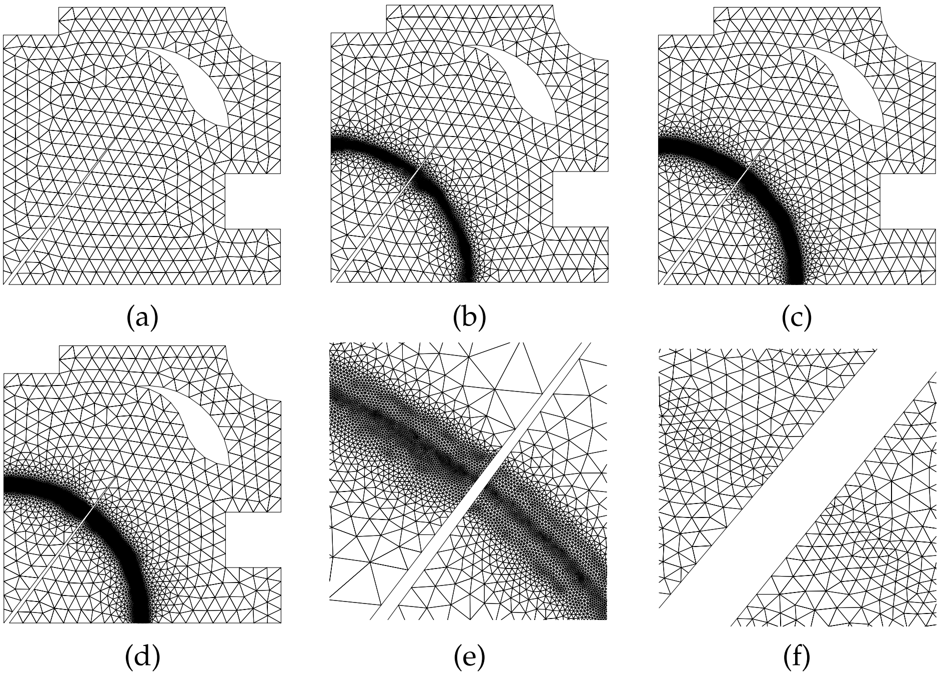

(a) (b) (c)

(d) (e) (f)

Figure 20: Adaptive CVDT meshes for the Experiment 4: (a) initial one; (b), (c), and (d) after 2, 6 and 10 refinements; (e), and (f) local views near the singularity region at the refinement level 6 and 10, respectively.

is solved with $a=1.0$, f and g are appropriately chosen such that the exact solution

$$u(x,y)=\exp\Big[-\frac{\big(\sqrt{x^2+y^2}-0.5\big)^2}{0.01^2}\Big],$$

from which it is clear that strong singularity occurs in the vicinity of the circle $x^2+y^2=0.25$.

Four adaptive meshes area shown in Fig. 20(a), (b), (c) and (d), respectively, and the statistics are contained in Table 13. The average mesh quality is up to 0.980, which demonstrates that the CVT-based meshing and optimization is robust in handling complicated geometry. This is also clearly shown in Fig. 20(e) and (f) which illustrate the high quality triangles of a zoomed portion of the final adaptive mesh around the singular area. The other data contained in Table 13 and the error distribution shown in Fig. 21

Table 13: Statistics of the mesh, finite element solution and error of Experiment 4.

level	N	Q_{avg}	Ψ	E_p	E_{melm}	$\|u_h-u\|$	$\|\|\|u_h-u\|\|\|$
0	459	0.981	0.627	—	1.9180	0.9732	16.53
2	3328	0.973	1.111	0.6224e-1	0.1407	0.2715e-2	1.8250
6	8981	0.978	1.059	0.1195e-1	0.2700e-1	0.7280e-3	0.9137
10	15285	0.981	1.038	0.5731e-2	0.1293e-1	0.4108e-3	0.6413

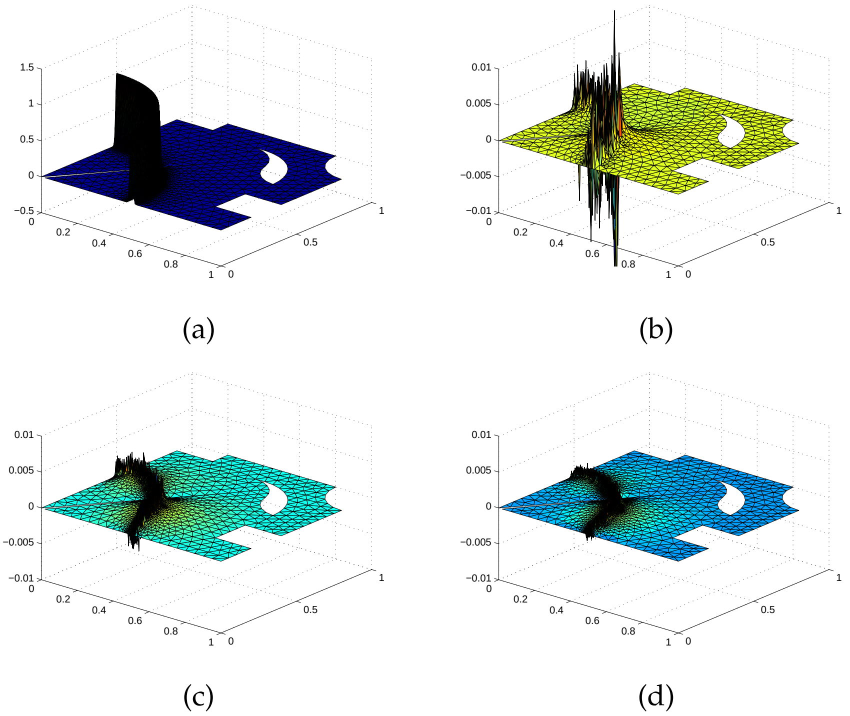
(a) (b) (c) (d)

Figure 21: Finite element solution and error distribution for the Experiment 4: (a) u_h on the 6th adaptive CVDT mesh; (b), (c), and (d) e_h corresponding to the adaptive CVDT mesh after 2, 6, 10 refinements, respectively.

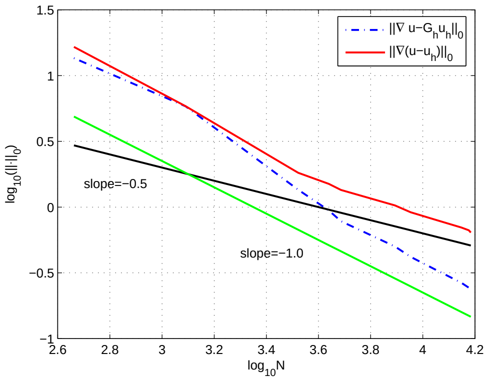

Figure 22: Quasi-optimality of the convergence rate of the adaptive FE procedure for the Experiment 4, where optimal decay is indicated by the line of slope -0.5.

clearly demonstrate that the adaptive FEM method is robust in handling singular problems with complicated geometries and curve singularity, which is further proved by the quasi-optimality indicated by the solid line shown in Fig. 22. The recovered energy error $\left(\|a^{-1/2}(G_h u_h - a\nabla u)\|_0\right)$ is presented as well by the dotted line which shown clearly the superconvergence property.

Experiment 5: With discontinuous coefficients. The final experiment is to solve Eq. (2.2) with a discontinuous coefficient a. Let $\Omega=[-1,1]$. $a(x,y)=1$, when $(x,y)\in\Omega_1\cup\Omega_3$, and $a(x,y)=161.447$, when $(x,y)\in\Omega_2\cup\Omega_4$. Here $\Omega_1=(-1,0)\times(0,1)$, $\Omega_2=(0,1)\times(0,1)$, $\Omega_3=(0,1)\times(-1,0)$, and $\Omega_4=(-1,0)\times(-1,0)$. The coefficient a is discontinuous across the x and y-axis. The problem was proposed by Kellogg in [30]. Let $f(x,y)=0$, then the exact solution u can be given (in polar coordinates) by $u(r,\theta)=r^\gamma\phi(\theta)$, where

$$\phi(\theta)=\begin{cases}\cos\Big(\Big(\dfrac{\pi}{2}-\sigma\Big)\gamma\Big)\cdot\cos\Big(\Big(\theta-\dfrac{\pi}{2}+\rho\Big)\gamma\Big), & \text{if } 0\le\theta\le\dfrac{\pi}{2},\\ \cos(\rho\gamma)\cdot\cos((\theta-\pi+\sigma)\gamma), & \text{if } \dfrac{\pi}{2}\le\theta\le\pi,\\ \cos(\sigma\gamma)\cdot\cos((\theta-\pi-\rho)\gamma), & \text{if } \pi\le\theta\le\dfrac{3\pi}{2},\\ \cos\Big(\Big(\dfrac{\pi}{2}-\rho\Big)\gamma\Big)\cdot\cos\Big(\Big(\theta-\dfrac{3\pi}{2}-\sigma\Big)\gamma\Big), & \text{if } \dfrac{3\pi}{2}\le\theta\le 2\pi.\end{cases}\tag{4.1}$$

Here, $\gamma=0.1$, $\rho=\pi/4$, and $\sigma=-14.922$.

The problem was considered by many authors [1, 10, 28]. To solve the problem via finite element method, the mesh is required to have no triangles violating the interface lines $x=0$ and $y=0$, in the sense that an edge-constrained triangular mesh should be constructed, so that the discontinuity of a only occurs across mesh edges. This can be easily realized via constrained boundary recovery [22] and constrained Delaunay insertion when points are added for mesh refinement and also it is easily built into the modified CVT-based meshing procedure discussed in Section 3.3.

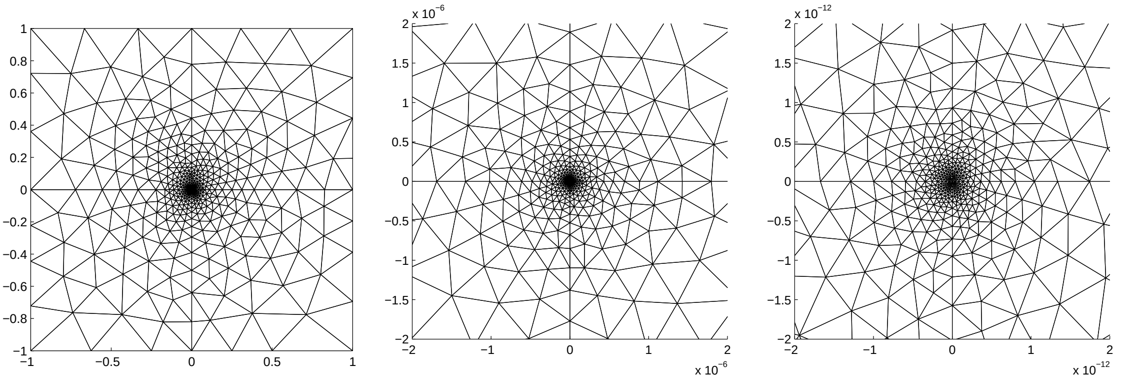

Figure 23: Adaptive mesh for the Experiment 5 (left) and two zoomed views.

Fig. 23 displays the adaptive meshes corresponding to the finest refinement level and the local zoomed views. The mesh is of high quality as in the previous examples. Similarly, the high quality results in superconvergent gradient recovery. It should be noted that the gradient recovery at an interface point should be done independently in each sub-domain and the minimal mesh size is taken as the sizing for the vertex. Accordingly, the effectiveness index of the a posteriori error estimation is also asymptotically close to 1.0, which leads to the convergence of the adaptive finite element solution procedure for the interface problem. The data are reported in Table 14. Fig. 24 shows the error distri-

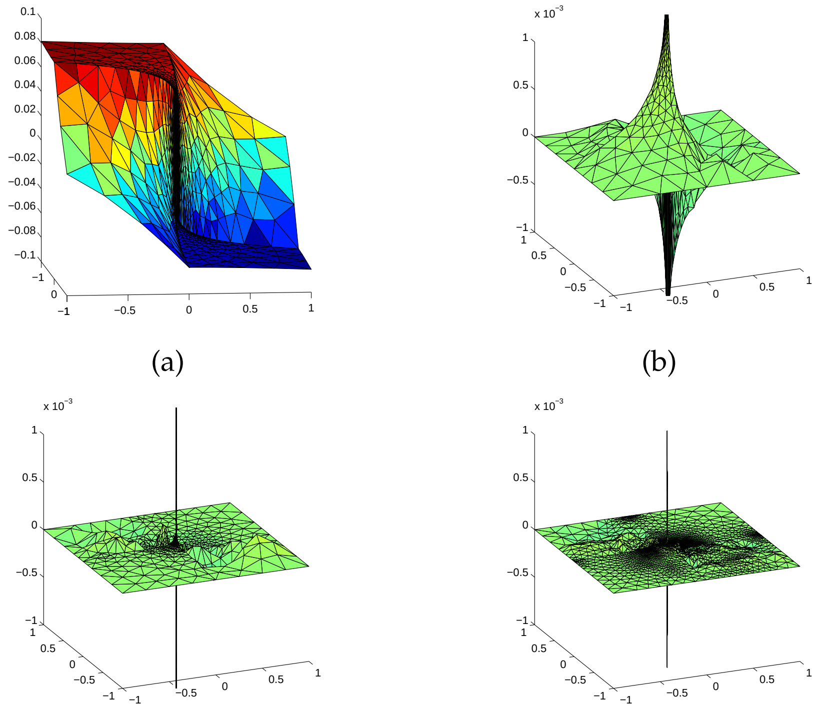

(a) (b)

(c) (d)

Figure 24: Finite element solution and error distribution for the Experiment 5: (a) u_h on the 40th adaptive CVDT mesh; (b), (c), and (d) e_h corresponding to the adaptive CVDT mesh after 9, 22, 40 refinements, respectively.

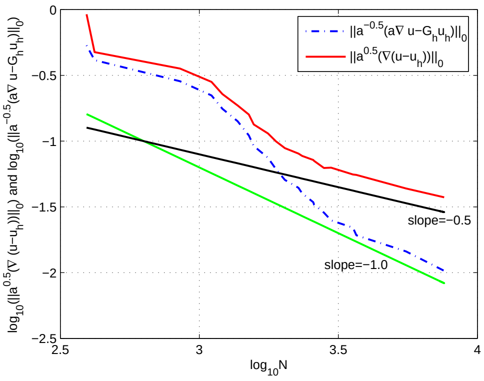

Figure 25: Quasi-optimality of the convergence rate of the adaptive FE procedure for the Experiment 5, where optimal decay is indicated by the line of slope -0.5.

bution which is almost equal over each element except that around the origin where the gradient is infinity. And quasi-optimality of the convergence order of the adaptation and the recovered energy error $\left(\|a^{-1/2}(G_h u_h - a\nabla u)\|_0\right)$ are obtained (see Fig. 25) as well.

Table 14: Statistics of the mesh, finite element solution and error of the Experiment 5 with extreme singularity.

level	N	Q_{avg}	Ψ	E_p	E_{melm}	$\|u-u_h\|$	$\|\|\|u_h-u\|\|\|$
0	393	0.978	0.413	—	0.175e-0	0.212e-3	0.922e-0
2	852	0.953	0.387	0.135e-1	0.387e-1	0.116e-4	0.356e-0
5	1373	0.954	0.507	0.566e-2	0.191e-1	0.111e-5	0.186e-0
10	2032	0.954	0.822	0.330e-2	0.115e-1	0.338e-7	0.884e-1
20	7592	0.964	0.956	0.670e-3	0.296e-2	0.572e-8	0.374e-1

5 Conclusions and future works

Various numerical experiments presented here demonstrate that the proposed CVT-based adaptive finite element method is robust and effective for the numerical solutions of elliptic equations with Dirichlet boundary conditions. Due to high quality mesh generation based on CVT, the classical gradient recovery ZZ-SPR enjoys nice superconvergence property which guarantees the asymptotical exactness of the a posteriori error estimation, as numerically substantiated by the effectiveness indices in all the conducted examples. The exactness guarantees the convergence of the whole adaptive procedure, which has been demonstrated by the quasi-optimality achieved in all the examples including the interface problem with discontinuous coefficients. The proposed adaptive FEM method has also been shown to be capable of handling complicated geometries.

For future works, the very first work is naturally that of conducting comparisons with methods proposed in [5–7, 28]. Other future working directions include the theoretical studies of the convergence of the adaptation procedure and the extension to three dimensional problems where a robust procedure for superconvergent gradient recovery on tetrahedral meshes may be developed, which has been under much recent investigations [37,42]. The applications of the method to time dependent and anisotropic problems are also interesting topics to be considered in the future.

Acknowledgments

The research of Huang is supported in part by the NSFC Key Project (11031006) and Hunan Provincial NSF Project (10JJ7001). The research of Qin is supported in part by Hunan Education Department Key Project 10A117. The research of Wang is supported in part by NTU star-up grant M58110011, MOE RG 59/08 M52110092 and NRF 2007IDM-IDM 002-010, Singapore. The research of Du is supported partially by NSF DMS-0712744 and NSF DMS-1016073.

References

[1] M. Ainsworth and J. T. Oden, A Posteriori Error Estimation in Finite Element Analysis, Wiley Interscience, New York, 2000.

[2] I. Babuška and T. Strouboulis, The Finite Element Method and Its Reliability, Numerical Mathematics and Scientific Computation, Oxford Science Publications, 2001.

[3] I. Babuška and A. Miller, A feedback finite element method with a posteriori error estimation: part I, the finite element method and some basis properties of the a posteriori error estimator, Comput. Meth. Appl. Mech. Engrg., 61 (1987), 1–40.

[4] I. Babuška and W. C. Rhcinboldt, A posteriori error estimates for the finite element method, Int. J. Numer. Method. Engrg., 12 (1978), 1597–1615.

[5] R. E. Bank and R. K. Smith, Mesh smoothing using a posterior error estimates, SIAM J. Numer. Anal., 34 (1997), 979–997.

[6] R. E. Bank and J. C. Xu, Asymptotically exact a posterior error estimates, part I: grids with superconvergence, SIAM J. Numer. Anal., 41 (2003), 2294–2312.

[7] R. E. Bank, PLTMG: A software package for solving elliptic partial differential equations users guide 10.0, department of mathematics, University of California at San Diego, 2007.

[8] C. Bernardi and R. Verf*ü*rth, Adaptive finite element methods for elliptic equations with nonsmooth coefficients, Numer. Math., 85 (2000), 579–608.

[9] S. C. Brenner and L. R. Scott, The Mathematical Theory of Finite Element Methods, Springer-Verlag, 1996.

[10] Z. M. Chen and S. B. Dai, On the efficiency of adaptive finite element methods for elliptic problems with discountinous coefficients, SIAM J. Sci. Comput., 24 (2002), 443–462.

[11] P. G. Ciarlet, The Finite Element Method for Elliptic Problems, North-Holland, Amsterdam, 1978.

[12] C. M. Chen and Y. Q. Huang, High Accuracy Theory of Finite Element Methods, Hunan Science Press, Hunan, China, 1995 (in Chinese).

[13] Q. Du, V. Faber and M. Gunzburger, Centroidal Voronoi Tessellations: applications and algorithms, SIAM Rev., 41 (1999), 637–676.

[14] Q. Du and M. Gunzburger, Grid generation and optimization based on Centroidal Voronoi Tessellations, Appl. Comput. Math., 133 (2002), 591–607.

[15] Q. Du and D. S. Wang, Tetrahedral mesh generation and optimization based on Centroidal Voronoi Tessellations, Int. J. Numer. Method. Engrg., 56 (2003), 1355–1373.

[16] Q. Du and D. Wang, On the optimal Centroidal Voronoi Tessellations and the Gersho's conjecture in the three dimensional space, Int. J. Comput. Math. Appl., 499 (2005), 1355–1373.

[17] Q. Du and D. Wang, Anisotropic Centroidal Voronoi Tessellations and their applications, SIAM. J. Sci. Comput., 26 (2005), 737–761.

[18] Q. Du and D. Wang, Mesh optimization based on Centroidal Voronoi Tessellation, Int. J. Numer. Anal. Model., 2 (2005), 100–114.

[19] Q. Du and L. Ju, Numerical simulation of the quantized vortices on a thin superconducting hollow sphere, J. Comput. Phys., 201 (2004), 511–530.

[20] J. J. Douglas and T. Dupont, Superconvergence for Galerkin methods for the two-point boundary problem via local projections, Numer. Math., 21 (1973), 270–278.

[21] Q. Du and L. Ju, Finite volume methods on spheres and spherical centroidal Voronoi meshes, SIAM J. Numer. Anal., 43 (2005), 1673–1692.

[22] Q. Du and D. Wang, Constrained boundary recovery for 3D Delaunay triangulations, Int. J. Numer. Method. Engrg., 61 (2004), 1471–1500.

[23] P. L. George and H. Borouchaki, Delaunay Triangulation and Meshing, Application to Finite Elements Methods, *Hermè*s, Paris, 1998.

[24] A. Zhou and Q. Lin, Optimal and superconvegence estimates of the finite element method for a scalar hyperbolic equation, Acta. Math. Sci., (English Ed.) 14 (1994), 90–94.

[25] N. Yan and A. Zhou, Gradient recovery type a posteriori error estimates for finite element approximations on irregular meshes, Comput. Methods. Appl. Mech. Engrg., 190 (2001), 4289–4299.

[26] G. Goodsell and J. R. Whiteman, A unified treatment of superconvergent recovered gradient functions for piecewise linear finite element approximations, Int. J. Num. Method. Engrg., 27 (1989), 469–481.

[27] Y. Huang, H. Qin and D. Wang, Centroidal Voronoi tessellation-based finite element superconvergence, Int. J. Numer. Method. Engrg., 76 (2008), 1819–1839.

[28] L. Ju, M. Gunzburger and W. D. Zhao, Adaptive finite element methods for elliptic PDEs based on conforming centroidal Voronoi Delaunay triangulations, SIAM J. Sci. Comput., 28 (2006), 2023–2053.

[29] M. Křížek, Superconvergence phenomena in the finite element method, Comput. Methods. Appl. Mech. Engrg., 116 (1994), 157–163.

[30] R. B. Kellogg, On the Poisson equation with intersecting interface, Appl. Anal., 4 (1975), 101–129.

[31] N. D. Levine, Superconvergent recovery of the gradient from piecewise linear finite element approximations, IMA J. Numer. Anal., 5 (1985), 407–427.

[32] A. M. Lakhany, I. Marek and J. R. Whiteman, Superconvergence results on midly structured triangulations, Comput. Methods. Appl. Mech. Engrg., 189 (2000), 1–75.

[33] R. Lin and Z. Zhang, Natural superconvergent points of triangular finite elements, Numer. Meth. PDEs., 20 (2004), 864–906.

[34] S. Lloyd, Least square quantization in PCM, IEEE T. Infom. Theory., 28 (1982), 129–137.

[35] P. Morin, R. H. Nochetto and K. G. Siebert, Data oscillation and convergence of adaptive FEM, SIAM J. Numer. Anal., 37 (2000), 466–488.

[36] A. Naga and Z. M. Zhang, A posteriori error estimates based on the polynomial preserving recovery, SIAM J. Numer. Anal., 42 (2004), 1780–1800.

[37] A. Naga and Z. M. Zhang, The polynomial-preserving recovery for higher order finite element methods in 2D and 3D, Dis. Cont. Dyn. B., 53 (2005), 769–798.

[38] R. Verfürth, A Review of a Posteriori Error Estimation and Adaptive Mesh-Refinement Techniques, New York, Wiley-Teubner, 1996.

[39] L. B. Wahlbin, Superconvergence in Galerkin Finite Element Methods, Volume 1605 of Lecture Notes in Mathematics, Springer, Berlin, 1995.

[40] D. Wang, O. Hassan, N. Weatherill and K. Morgan, Enhanced remeshing from STL files and its application to surface grid generation, Commun. Numer. Methods. Engrg., 23 (2007), 227–239.

[41] D. Watson, Computing the n-dimensional Delaunay tessellation with applications to Voronoi polytopes, Comput. J., 24 (1981), 167–172.

[42] H. Wu and Z. M. Zhang, Can we have superconvergent gradient recovery under adaptive meshes, SIAM J. Numer. Anal., 45 (2007), 1701–1722.

[43] J. C. Xu and Z. M. Zhang, Analysis of recovery types a posteriori estimators for middly structured grids, Math. Comput., 73 (2004), 1139–1152.

[44] J. Z. Zhu and O. C. Zienkiewwicz, Superconvergence recovery technique and a posteriori error estimators, Int. J. Numer. Method. Engrg., 30 (1990), 1321–1339.

[45] O. C. Zienkiewicz and J. Z. Zhu, A simple error estimator and adaptive procedure for practical engineering analysis, Int. J. Numer. Method. Engrg., 24 (1987), 337–357.

[46] O. C. Zienkiewicz and J. Z. Zhu, The superconvergent patch recovery (SPR) and adaptive finite element refinement, Comput. Methods. Appl. Mech. Engrg., 101 (1992), 207–224.